Grain size effect on strain localization, slip-grain boundary interaction and damage in the Alloy 718 Ni-based superalloy at 650 °C

Malo Jullien, R.L. Black, Jean Charles Stinville, Marc Legros, Damien Texier

Grain size effect on strain localization, slip-grain boundary interaction and damage in the Alloy 718 Ni-based superalloy at 650 °C

Malo Jullien[a,b,*], R. L. Black[c], J. C. Stinville[c], Marc Legros[b], Damien Texier[a,*]

[a] *Institut Clement Ader (ICA) - UMR CNRS 5312, Université de Toulouse, CNRS, INSA, UPS, Mines Albi, ISAE-SUPAERO, Campus Jarlard, 81013 Albi Cedex 09, France*
[b] *Centre d'Elaboration de Matériaux et d'Etudes Structurales, CNRS UPR 8011, 31055 Toulouse cedex 4, France*
[c] *University of Illinois Urbana-Champaign, Urbana, IL, USA*

Abstract

Grain size effects on the early plastic strain localization and slip transfer at grain boundaries were investigated for the Alloy 718 Ni-based superalloy at 650 °C. Three microstructures with different grain sizes underwent monotonic tensile tests at 650 °C, both in air and under vacuum, until rupture. All the microstructure variants exhibit fully intragranular fracture under vacuum and partially intergranular fracture in air. In this latter case, predominant intergranular fracture mode was found in the fine-grain microstructures. Interrupted tensile tests were also conducted under vacuum with *ex-situ* SEM high-resolution digital image correlation (HR-DIC) measurements to assess in-plane kinematics fields at the microstructure scale. Out-of-plane displacement jumps were obtained using laser scanning confocal microscopy. Both crystallographic slip within grains and near Σ3 twin boundaries (TBs) and morphological sliding happening at grain boundaries (GBs) were documented. Statistical analysis of all plastic events aimed at quantifying strain localization distribution as a function of the microstructure. The fine-grain microstructure was found to have extensive strain localization at grain boundaries, while the coarse-grain microstructure is more prone to intragranular slip development and slip localization near TBs. Different scenarios of slip band/grain boundary interactions were evidenced.

Keywords: Digital image correlation, Nickel-based superalloy, Slip activity, Grain boundary sliding, Grain size effect, Slip transfer

1. INTRODUCTION

Alloy 718 is a Ni-based superalloy widely used in the hot sections of aerospace, marine and nuclear turbines. Extensive works were done on this material during decades of use to continuously enhance its mechanical and corrosion resistance properties, playing on its chemistry, its microstructure (typically grain size), its precipitation state, its residual deformation state inherited from various thermomechanical processing routes. Engineering and research developments have pushed this material to its limit, offering a very good trade-off material in terms of economical and technical characteristics in its wrought polycrystalline form. It is therefore important to understand the influence of microstructural features on its mechanical behavior under extreme environments. Grain boundaries (GBs) are often considered as the weak point of polycrystalline alloys at high temperature, acting as the preferential path for oxygen diffusion [1]. Intergranular oxidation of Alloy 718 in air has been documented and analyzed at temperatures ranging from intermediate to high temperature in the past [2]. This phenomenon negatively impacts the lifespan of parts in service due to its tendency to cause premature intergranular cracking. The phenomenon of oxidation-assisted intergranular cracking (OAIC) was extensively studied for Alloy 718 during the past decades [3, 4, 5]. There is a consensus on a two-range effect of oxygen [1]: a short-distance effect characterized by oxide formation at GBs, and a long-distance effect arising from oxygen diffusion at GBs, which can lead to the creation of embrittling elements. Oxygen reacts at GBs in Alloys 718 with alloying elements, particularly with niobium, to form brittle oxides. This

*Corresponding author
Email addresses: malo.jullien@mines-albi.fr (Malo Jullien), damien.texier@mines-albi.fr (Damien Texier)

results in a change of fracture mode from intragranular to intergranular and significantly increases crack propagation rates [6, 7].
In addition to being key contributors to damage behavior at high temperatures, GBs also significantly influence the deformation processes of polycrystalline alloys. Their influence on the elastic limit and hardening law at the macroscopic scale is well established, most notably through the Hall-Petch relation [8, 9, 10]. At the microstructure level, GBs induces plastic incompatibilities and heterogeneous deformation [11]. Nye introduced the concept of geometrically necessary dislocations (GNDs) to account for plastic bending in a crystal. The density of these GNDs can be quantified by using high-resolution Electron Backscatter Diffraction (EBSD) techniques, helping quantify such heterogeneous deformation. Grain reorientation through GB accommodation was identified using this tool on nickel-based superalloys subjected to high temperature creep solicitations [12]. It also enabled to evidence the accommodation of slip bands by grain boundaries on commercial purity titanium alloys [13], aluminum [14], steel [15] or Ni-based superalloys [16, 17]. In addition, new techniques such as high resolution-digital image correlation (HR-DIC) [18, 19, 20, 21, 22] and laser scanning confocal microscopy (LSCM) [15, 23] enable to assess both in-plane and out-of-plane components of the strain field. It opens new perspectives to quantitatively characterize both crystallographic slip (intragranular slip) and morphological sliding occurring at GBs at high temperature.
To mitigate their sensitivity to oxidation, grain boundary engineering was used [24]. In the case of Alloy 718, annealed twin boundaries (TBs) of type $\Sigma 3$ have shown to have a higher resistance to high temperature oxidation than conventional GBs [25]. However, at room temperature, TBs were also found to be preferred crack initiation sites, especially under cyclic loading [26, 27, 28, 23]. This was attributed to intense strain localization near and parallel to TBs [29, 30]. Grain size effects were also investigated in the literature on the crystal plasticity behavior of a 316L stainless steel, considering slip localization/grain boundary interactions [31]. In a preliminary study [32], the strain localization behavior of the Alloy 718 Ni-based superalloy was investigated from room temperature up to 650 °C. While almost no strain localization was found at GBs for temperatures ranging from room temperature to 350 °C, a competition between strain localization at TBs, GBs, and the interior of the grains was demonstrated at 650 °C. This recent work evidenced the development of early damage at grain boundaries either due to the contribution of adjacent slip localization events developing near and parallel to twin boundaries or special kinematics stresses at grain boundaries (mode I stress) leading to cavitation at grain boundaries. This cavitation phenomenon at grain boundaries was also modeled for Alloy 718 at 650 °C considering a crystal plasticity model combined with grain boundary cavity model [33]. However, the sensitivity of strain partitioning at the microstructure level as a function of microstructural features such as grain size was not investigated, despite important needs in material design.
Furthermore, intragranular slip activity as well as slip transfer at general grain boundaries and annealed twin boundaries for the Alloy 718 was recently investigated at 650 °C *in-situ* in a SEM [16]. The authors used a combination of slip traces analysis method, EBSD characterizations, and crystal plasticity finite element method to document slip transfer at grain boundaries and propose a morphological and crystallographic criterion to predict induced activated slip systems. However, slip/grain boundary interaction at high temperature; when grain boundaries have the ability to slide; has not been reported for such material and is central in the present investigation.
Grain size and grain boundary issues have been central to the study of the mechanical behavior of polycrystalline materials [10, 17, 33, 34, 32]. The present work aims to address the influence of the grain size on the strain localization at the microstructure scale, slip-grain boundary interaction, early damage development, and fracture. HR-DIC was conducted on three different grain-size materials that underwent interrupted tensile tests at 650 °C under protective environment. A statistical analysis was performed to quantify strain localization at the different microstructural features. In parallel, specific cases of interactions between slip bands and GBs were analyzed individually. The results are correlated with the fracture behavior observed for the different grain sizes during tensile test at 650 °C in air and under vacuum.

2. MATERIAL & METHODS

2.1. Material

The material investigated in the present study is a wrought Alloy 718 of the following nominal composition: Bal. Ni, 18.57 % Cr, 18 % Fe, 5.02 % Nb, 2.86 % Mo, 0.11 % Co, 0.58 % Al, 0.97 % Ti, <0.01 % Ta (weight percent). The as-received rolled sheet was in a solid solution state (γ phase-state). Three sets of samples were laser-machined

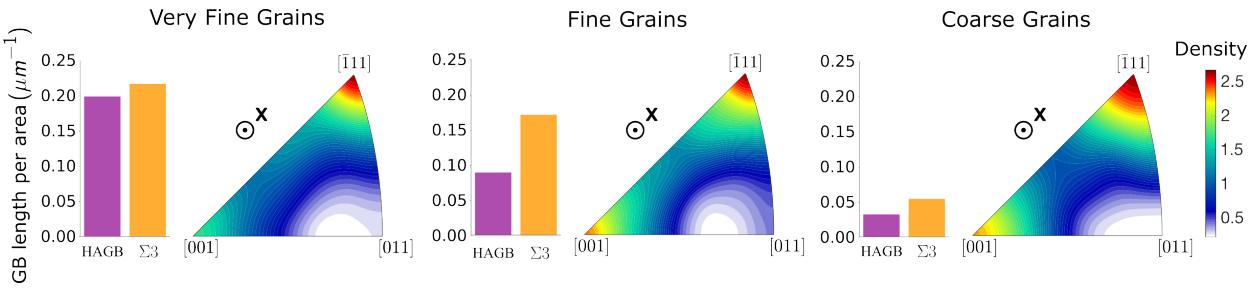

Figure 1: Grain boundaries and orientations along the loading direction (X) distributions for each microstructure.

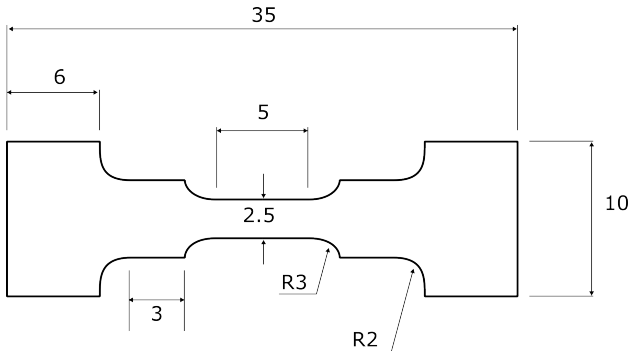

Figure 2: Geometry of the tensile specimens (dimensions in mm)

from a 635 μm-thick rolled sheet. The geometry of the tensile specimens is illustrated in Figure 2. Two sets of them underwent a 1080 °C grain growth heat treatment, one for 5 minutes (Fine-grain (FG) microstructure) and the other for 5 hours (Coarse-grain (CG) microstructure). They resulted in an average grain size of 40 μm and 100 μm, respectively. The as-received material (Very fine-grain (VFG) microstructure) has an average grain size of 12 μm. Following the grain growth heat treatment, a two-step aging heat treatment at 720 °C then 620 °C, both for 8 hours, was applied to different materials variants. It resulted in a γ / γ' / γ'' microstructure (No δ phase). As depicted in Figure 1, all the microstructure variants present similar texture, with the [111] and [001] directions as preferred orientations along the loading direction.The length of grain boundary per surface area was also calculated for all the microstructure variants and was illustrated in Figure 1. No low angle grain boundaries (LAGB) were found on either of the microstructure variants. The length of Σ3 twin boundaries (Σ3 TB) is compared to the length of high angle grain boundaries (HAGB). As expected, the proportion of GB per surface area decrease with the grain size. The very fine grain, the fine grain and the coarse grain microstructures have a fraction of Σ3 boundaries of 52%, 66% and 63%, respectively.

All the samples were mechanically ground using SiC papers, then polished with diamond paste and surface-finished with colloidal silica. Two kinds of speckle pattern were applied, one for optical macroscopic DIC and another for high-resolution DIC (HR-DIC). The macroscopic speckle is plaster sputtering, which randomly distributes small cement particles (a few microns) at the surface of the samples. This speckle patterning technique was used as an optical extensometer to measure the sample elongation during tensile test up to failure (as used in Ref [35]). It is stable both in air and under vacuum for hours at 650 °C. The speckle pattern for high-resolution purposes was only applied on the samples for interrupted tensile tests. It is a natural speckle formed using a short-term pre-oxidation of Alloy 718 at 650 °C for 15 minutes in air. A thin layer of oxide was formed. The resulting speckle pattern has a randomly distributed gray level, copying the γ / γ' / γ'' microstructure of Alloy 718. This speckle pattern enables sub-grain measurement of the kinematics field compatible with dissociation of distinct microplasticity events far from 600 nm, as demonstrated in [32]. In addition, the macroscopic heterogeneity of the oxide layer also enables to perform standard DIC. This speckle is also stable under a protective environment for hours at 650 °C.

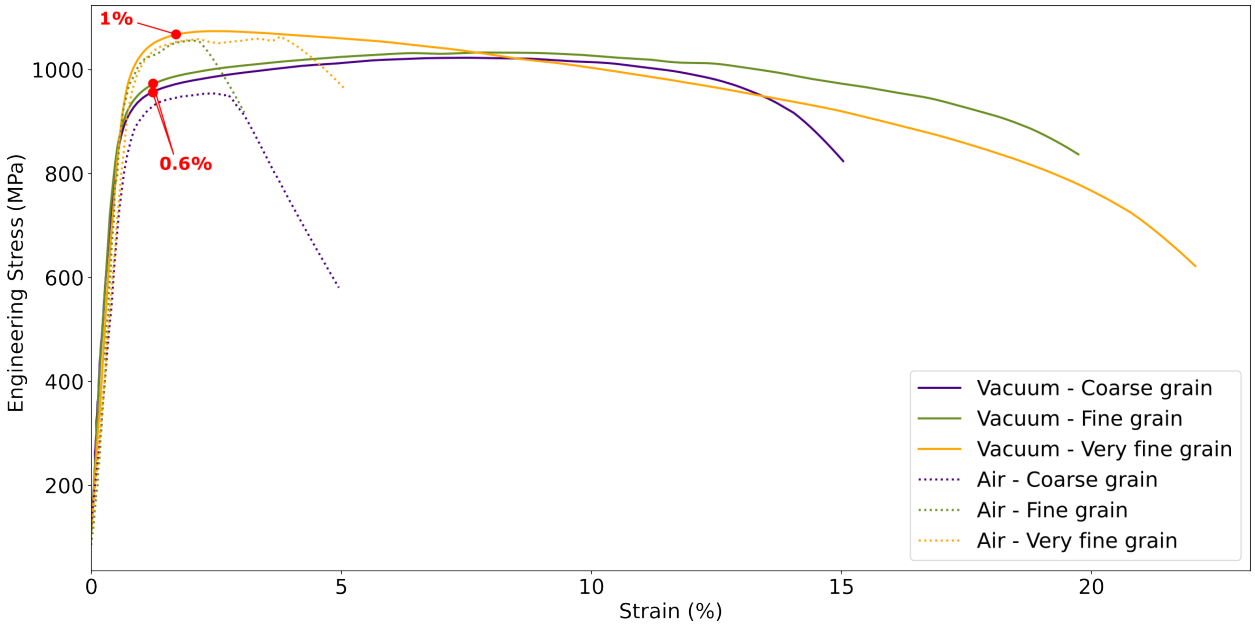

Figure 3: Engineering stress-strain curves of the investigated materials in air and under vacuum. Dotted lines stand for the tests under air, and solid lines for the tests under vacuum. Red dots are located at the interruption location for HR-DIC purposes.

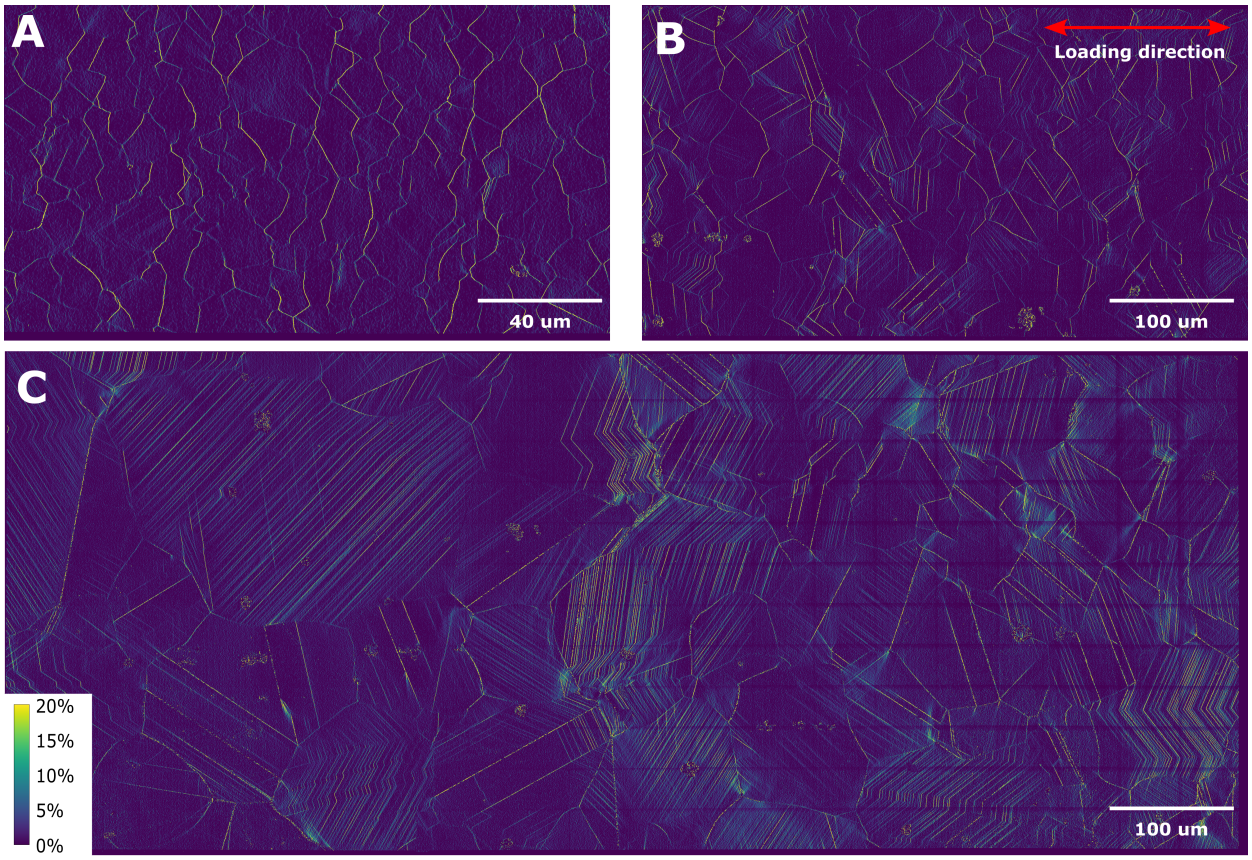

Figure 4: Strain maps obtained by HR-DIC; A. Very fine-grain microstructure; B. Fine-grain microstructure; C. Coarse-grain microstructure

2.2. Tensile tests

For this work, a total of nine tensile tests were conducted. Three configurations were used, each with the three grain sizes: (1) up-to-failure tests in air, (2) up-to-failure tests under vacuum, and (3) interrupted tests under vacuum. All tests were performed at 650 °C with a strain rate of 10^{-4} s^{-1} and interrupted tensile tests were stopped at 1% of plastic strain for the very fine grains microstructure and 0.6% for the fine and coarse microstructures. Tensile specimens had a dog-bone-like geometry, which dimensions are exposed on Figure 2. The sample was heated using a resistive furnace with a center split design centered on a quartz tube, isolating the sample from laboratory air. Tensile curves were plotted using macroscopic DIC from images taken at regular intervals with an optical Basler camera, as shown in Figure 3.
HR-DIC was only used for the interrupted tests. For this latter technique, the images are high-resolution SEM micrographs captured *ex-situ* before and after interruption with a FEI Helios 600i. For both samples, the reconstructed mosaic from SEM micrographs covers a large area: 1×0.4 mm^2 for the coarse-grain microstructure and 1×0.3 mm^2 for the very fine- and fine-grain microstructures. HR-DIC calculations were performed on individual images using the Heaviside-DIC method [22], and portions of the resulting strain fields are shown in Figure 4. Out-of-plane measurements were also performed *ex-situ* using an Olympus LSCM (LEXT OLS5100). This technique was used to map the entire sample gauge topography. The topography map has a lower in-plane spatial resolution than SEM (only 120 nm) but a Z-resolution of 9 nm. Finally, EBSD maps obtained with a JEOL JSM 7100F SEM and an Oxford EBSD SYMMETRY S2 system were incorporated into the dataset.

2.3. Statistical analysis

The size of the collected dataset allows for a reliable statistical analysis with the goal of capturing temperature and environmental dependencies on strain localization. Figure 5 shows a portion of this dataset. The measurements performed and previously mentioned yielded the following data:

- The in-plane strain field provided by the HR-DIC (see Figure 5.A).
- The crystallographic texture and GB information such as misorientation from EBSD measurements (Figure 5.B).
- The in-plane displacement amplitude at discontinuities obtained using the Heaviside-DIC technique. It is measured as the jump between the two displacement fields on each side of the discontinuity (Figure 5.C).
- The in-plane displacement direction at discontinuities obtained using the Heaviside-DIC technique. Using this information and the grain orientation provided by the EBSD, it is possible to either identify the slip system activated (projection of the cumulative Burgers vector onto the sample surface) or to state if the strain localization follows a unique slip plane or not (necessary also for morphological sliding).
- The out-of-plane displacement amplitude provided by the height map captured using LSCM (Figure 5.E).

By comparing in-plane and out-of-plane measurements, it is possible to identify both crystallographic and morphological sliding. To compare the various data, the maps were aligned using a control point method from the Argos package [36]. Once the maps were aligned, zones or events of interest were manually identified on the strain map (manual segmentation and labeling of the strain localization events). ImageJ tools were used to collect the corresponding data on each component of the dataset [37]. An example of collected data along a TB is exposed on Figures 5.D and F. Figure 5.C and D show an example of in-plane displacement collected along a TB (overlaid with a white arrow). This same TB is highlighted on the strain field and the EBSD map in Figure 5.A and B, respectively. The EBSD data also serves as a mean to associate and classify plastic events with a microstructural location: (1) Non-straight events and events located close to a GB (distance less than 1.2 μm) are classified as GB sliding; (2) straight events located closer than 1.2 μm to a TB are classified as slip near TB; (3) and all others are classified as intragranular slip since they occur in the grain interior. The 1.2 μm value used for the classification was determined taking into account: (i) the fact that slip occurs near TBs and not at TBs [30]; (ii) despite its size, the quality of the dataset leads to very low misalignment between EBSD data and mechanical maps. Series of tests were conducted to find the lowest value certifying the right classification of the events. This procedure generates a database, which is then used to perform statistical analysis using a home-developed Python script.

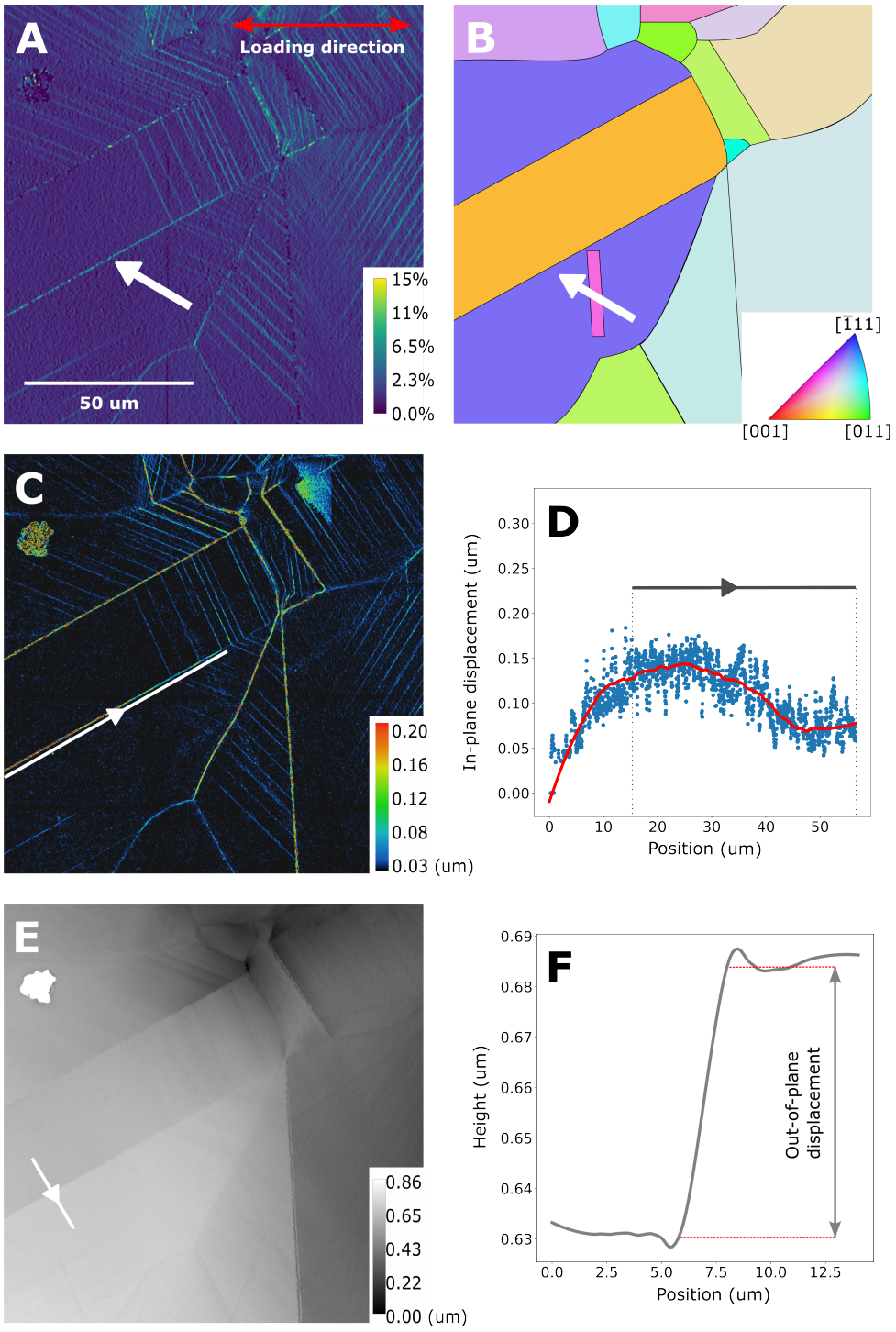

Figure 5: A. Strain map of a region of interest obtained by HR-DIC; B. EBSD of the corresponding area; C. Slip amplitude map obtained by HR-DIC; D. Plot along the white arrow in Figure C. It corresponds to the slip amplitude along the selected twin boundary; E. Height map obtained by LSCM; F. Plot along the white arrow on figure E. giving the out-of-plane step corresponding to the slip band activated near the selected twin boundary.

3. RESULTS

3.1. Tensile behavior

Tensile tests were performed under vacuum and in air at 650 °C for the different grain-size materials. Stress-strain curves resulting from the tensile tests up to failure are illustrated in Figure 3. Under vacuum, the very fine grain microstructure exhibits the higher yield strength, this latter tensile properties decreasing with the grain size. In the plastic regime, while the fine- and coarse- grain microstructures experience a similar work-hardening prior to the ultimate tensile strength in a large plastic domain (around 8 % plastic strain), the very fine-grain microstructure reaches the ultimate tensile stress at 1 % plastic strain then a progressive softening. It is worth mentioning the ductility of the specimens decreased with the grain size. To emphasize the environmental effects, the ductility was considered herein as the strain-to-failure, as commonly adopted in the stress-corrosion community. This criterion takes into account both the deformation and the damaging/failure behavior. Switching from vacuum to air results in a significant loss of ductility for all the microstructure variants. The ductility reduction is much greater for the fine- and very fine-grain microstructures than for the coarse-grain one (16 % against 10 % strain-to-failure difference). Ultimately, the coarse-grain microstructure, which is less ductile under vacuum, is more ductile than the fine microstructure under air conditions. According to the tensile curves, the very fine- and fine-grain microstructures are more affected by oxygen embrittlement than the coarse-grain microstructure.

The fracture surface of all the samples was analyzed post-mortem. The ones of the samples subjected to tensile tests under vacuum exhibited fully intragranular fracture behavior regardless of the grain size microstructure (not presented in the article). In contrast, fracture behavior in air is partially intergranular. Figures 6.A, D and E are SEM micrographs covering the entire fracture surfaces of the very fine-, coarse- and fine-grain microstructure, respectively. According to the fracture surfaces, the fraction of intergranular fracture is similar for the fine- and very fine-grain microstructures (29 % and 28 % of the entire fracture surface). However, only 18 % of the fracture surface of the coarse-grain microstructure is intergranular. This fraction of intergranular fracture is measured from fracture surface images shown in Figures 6.A, D and E. It corresponds to the area covered by intergranular fracture divided by the gauge section area. It is worth mentioning that, the fine-grain fracture surface (Figure 6.D) results from the propagation of two initiation sites when the very fine-grain and coarse-grain fracture surfaces (Figure 6.A and E) result from the propagation of a single initiation site. A closer examination of the intergranular fracture regions (Figure 6.B, C and G) reveals GB decohesion on all the microstructure variants. In addition, an increasing slip band density was observed at the grain surface with the increasing grain size. Interestingly, several features corresponding to the presence of strain localization at TBs were observed in the intergranular regions; two being indicated by the arrows in Figure 6.B and C. Moreover, a case of decohesion between a GB and two TBs was found and pointed out by a double arrow in Figure 6.F. This evidences intense plastic activity at these features.

3.2. High resolution digital image correlation (HR-DIC) and statistical analysis

The strain fields shown in Figure 4 are the result of the HR-DIC calculation performed on interrupted tensile tests. The overall view provided by the map sizes reveals homogeneous behavior within each sample. Strain localization can be found on the three microstructure variants at the GB and inside the grains. However, significant differences in strain localization can be spotted on these strain maps. On the one hand, the coarse-grain microstructure (Figure 4.C) experienced more intragranular slip bands than the fine- and very fine-grain microstructures (Figure 4.B and A). On the other hand, the very fine-grain microstructure has an intense and dense strain localization at GB. A statistical analysis was performed to investigate strain localization further. To achieve this, 1574, 1304, and 1318 plastic localization events (intragranular slip or grain boundary sliding) for the coarse-, fine- and very fine-grain microstructures were identified, respectively. The classification of these events is shown in the histogram in Figure 7. The height of the bars corresponds to the slip density measured on HR-DIC maps. The latter is the amount of slip per area, which can be estimated as: $A = \sqrt{b_{IP}^2 + b_{OP}^2} * L$

b_{IP} and b_{OP} being the in-plane and out-of-plane projection of the slip displacement vector, respectively; one is measured with the HR-DIC and the other with LSCM. These are represented on Figure 9. L is the length of the plastic event.

The very fine grain microstructure has a higher slip density than the others microstructures. This result was expected because the very fine microstructure test was stopped at 1 % plastic strain versus 0.6 % for the others microstructures.

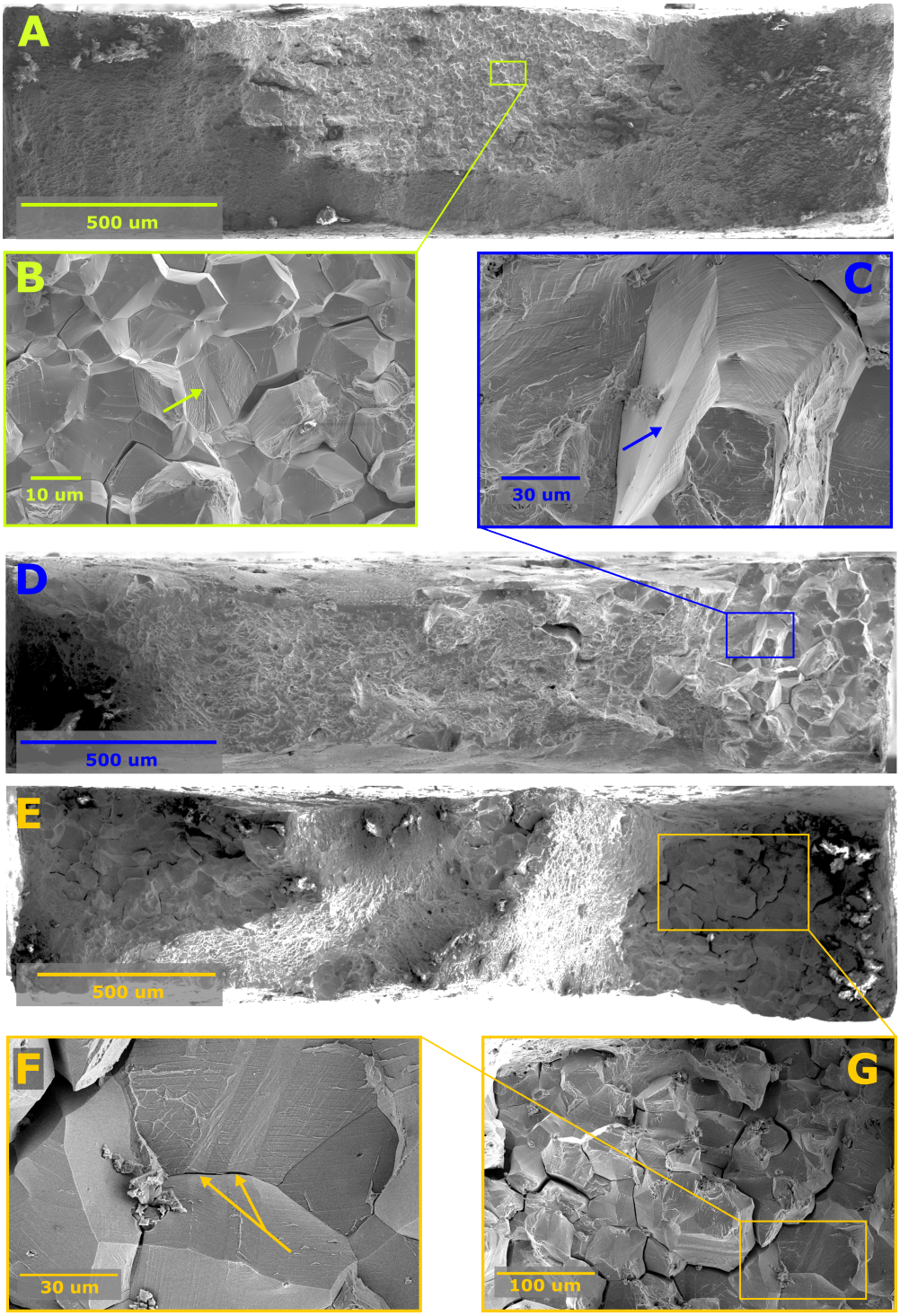

Figure 6: SEM images of the fracture surfaces. A, D and E images are the entire fracture surfaces of the very fine, coarse and fine grains microstructure, respectively. B, C, F and G are magnifications of the fracture surfaces.

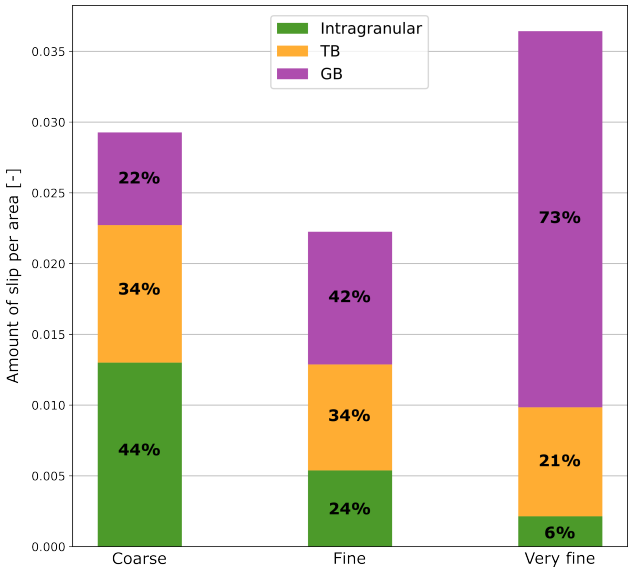

Figure 7: Amount of strain localization per area for each microstructure and their distribution between microstructural features.

However, a greater amount of slip per area was found for the coarse-grain microstructure compared to the fine-grain microstructure. This shows a greater amount of unlocalized strain in the fine-grain microstructure. The composition of each slip density, however, differs between the microstructures. It was found that a fine-grain size favors GB sliding, while a coarser grain size favors intragranular slip. Indeed, for the very fine-grain microstructure, 73 % of the amount of slip is located at GBs against only 6 % at the interior of grains. For the coarse-grain microstructure, the opposite is true, *i.e.*, only 22 % of the amount of slip is located at GBs against 44 % at the interior of grains. The fine-grain microstructure is in between, 42 % of the amount of slip is located at GBs against 24 % at the interior of grains. Like the amount of slip at the interior of grains, the amount of slip localization near TBs is also decreasing with the decreasing grain size but to a lesser extent. It accounts for a significant share in all microstructures studied, accounting for 34 %, 34 % and 21 % of the total amount of slip amount for the coarse, fine and very fine grain microstructures, respectively.

Differences in intensity between microstructural features can be seen when looking at strain fields shown in Figure 4. To highlight these differences, the probability density function (PDF) was interpolated from the data collected using Python's SciPy library. The plot of the PDF as a function of the intensity of the slip amplitude is shown in Figure 8. This graph depicts the distribution of events based on their amplitude. The gray curve accounts for all plastic events, whereas the colored curves only account for one type of microstructural feature. Vertical dotted lines represent the median intensity values. When all events are considered, the finer the grains, the higher the median intensity and the greater the scatter. However, at equivalent strain level (0.6 % plastic strain for the coarse-grain and fine-grain microstructures) a coarser microstructure has a higher maximum intensity (0.85 μm versus 0.64 μm). The very fine-grain microstructure deformed at 1 % plastic strain has a lower maximum intensity compared to the coarse-grain microstructure deformed at 0.6 % plastic strain. Looking at the strain localization at TBs and GBs, they have about the same average intensity for each microstructure. Again, for all the microstructure variants, the strain intensity in the grain interior is lower compared to strain located at GBs and TBs. It is more pronounced in the coarse-grain microstructure, where the first quartile contains 93 % of intragranular slip events (versus 60 % for the fine-grain microstructure). When only the 100 most intense events are considered (pie charts Figure 8), the distribution of microstructural features differs from the overall distribution (Figure 7). For each microstructure studied, a higher proportion of strain localization is observed at TBs. These differences are more pronounced for the coarse- and fine-grain microstructures, where the proportion of strain localization at TBs is 32 % and 29 % higher among the 100 most intense events against 3 % for very fine-grain microstructure. This emphasizes how slip near TBs is intense. The proportion of strain localization at GBs within the 100 most intense-event category is similar to the one when considering all the events. This shows that grain boundary sliding events are well distributed in slip amplitude and are key features in the deformation

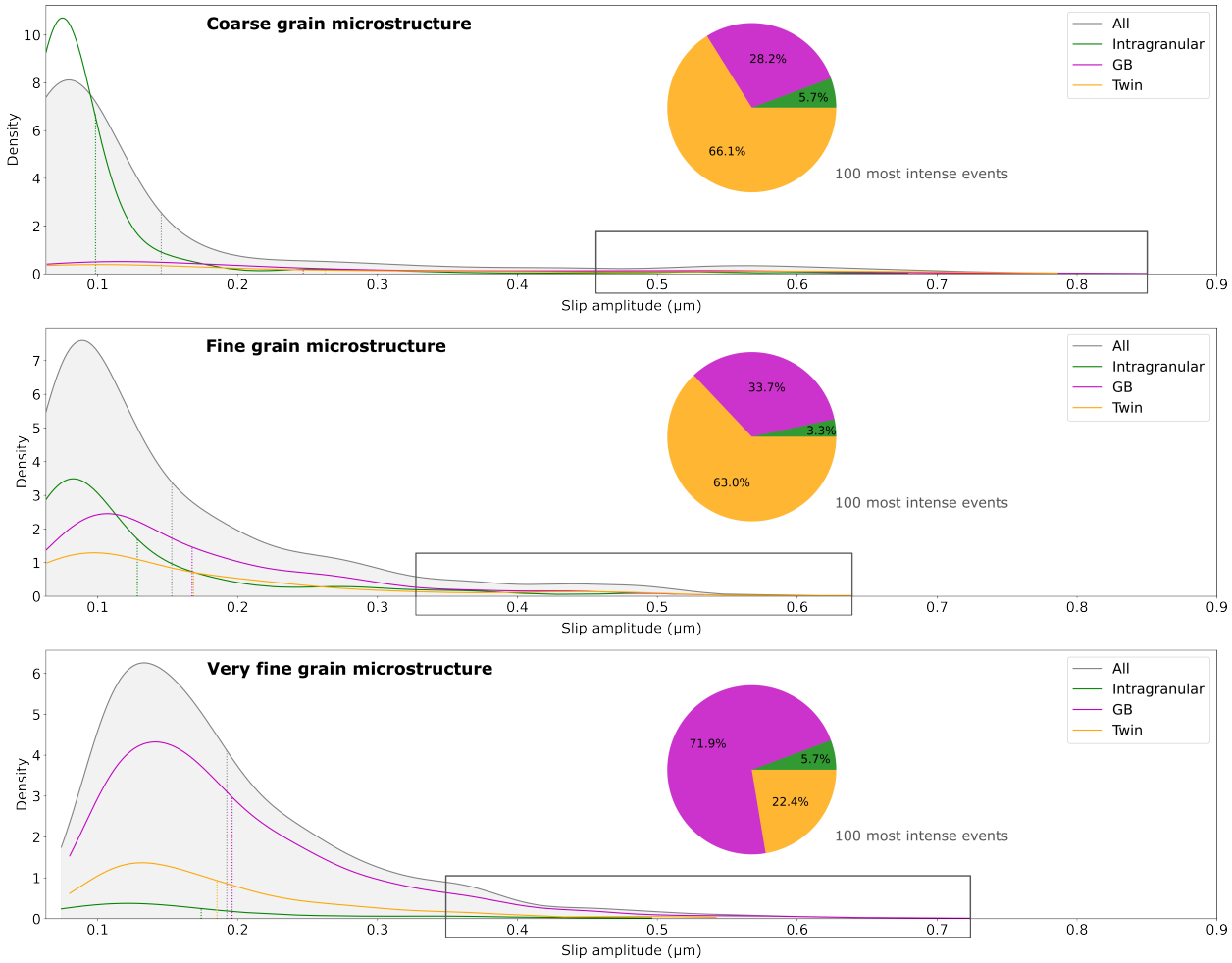

Figure 8: Distribution of the plastic events as a function of their slip amplitude. The distributions of all the events, depending on their location, are plotted in gray and in color, respectively. The dotted lines correspond to the average intensity values for each plot. The pie chart is a plot of the distribution of the amount of strain localization of the 100 most intense events (framed on the main plot).

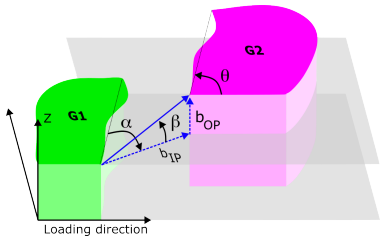

Figure 9: Schematic grain boundary sliding. θ is the angle between the loading direction and the GB; α is the direction of slip in the plane of the surface sample; β is the angle defining the out-of-plane direction of the slip.

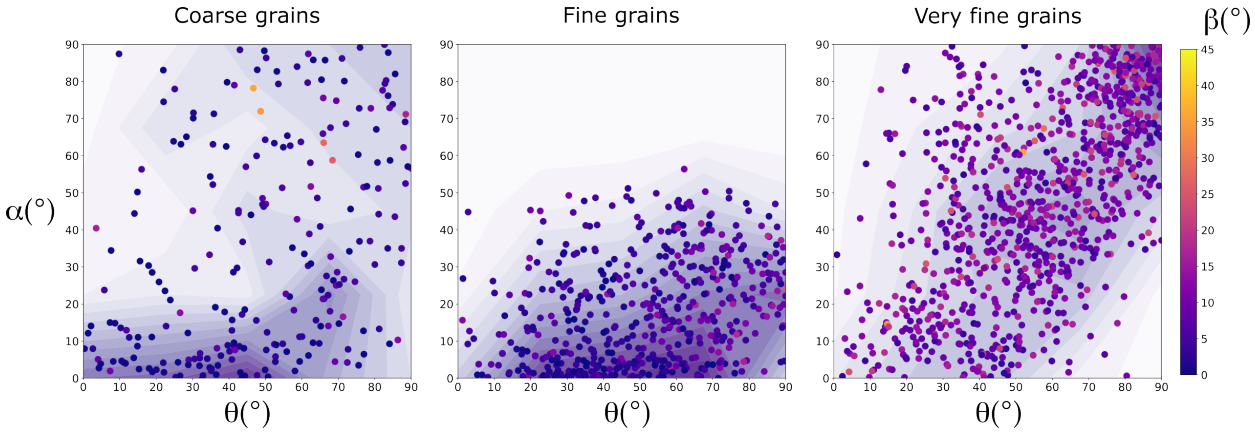

Figure 10: Grain boundary sliding characterization; Each point is a grain boundary sliding event plotted on the α/θ map. Angles are defined in the schematic illustration in Figure 9. A θ angle of 0 ° accounts of a GB parallel to the loading direction, and an α angle of 0 ° accounts for pure shearing. The color of the points indicates the out of plane nature of the slip event. The warmer the color, the more out-of-plane the slip is. The background is the density of the dots. The darker the color, the higher the density.

process at 650 °C. Finally, the strain localization at the interior of grains is very poorly represented within the 100 most intense-event category in each microstructure.

3.3. Grain boundary sliding characterization

A significant number of GB sliding was observed on both microstructures. This section will statistically investigate several GB sliding parameters to understand better their role in the deformation and damaging process. For better reading, several angles were given a name in the case of this study, as indicated in Figure 9. First, the direction of the GB towards the loading direction is given by the θ. If $\theta = 0$, the GB is parallel to the loading direction and if $\theta = 90$, the GB is orthogonal to the loading direction. Second, GB sliding is the displacement of a grain relative to another. This displacement is three-dimensional and can therefore be divided into the in-plane displacement ($\vec{b_{IP}}$) and the out-of-plane displacement ($\vec{b_{OP}}$). In this study, both displacement were measured using HR-DIC and LSCM measurements, respectively. The in-plane and out-of-plane displacement directions are given by the angles α and β, respectively. If both angles are equal to 0 ° the GB sliding is pure in-plane shearing.
In Figure 10, each GB sliding events have been plotted in the α/θ map, for each microstructure. The event density is plotted in the background of the maps. A darker area implies a higher density of events. For each microstructure, the points are scattered along the x-direction (θ angle). This indicates that strain localization can be found at GBs regardless of their orientation relative to the loading direction. However, in the case of the very fine-grain microstructure, a cluster can be found for the θ angles near 90 °. This means that in the very fine-grain microstructure, more strain localization can be found at the GBs orthogonal to the loading direction. Also, on the very fine-grain microstructure, it appears that the points are clustered around the $\alpha = \theta$ axis. On this axis, the in-plane direction of slip is aligned with the loading direction. Compared to the very fine grain microstructure where the in-plane sliding direction is close from the loading direction, the distribution pattern is different in the case of the coarse- and fine-grain microstructure.

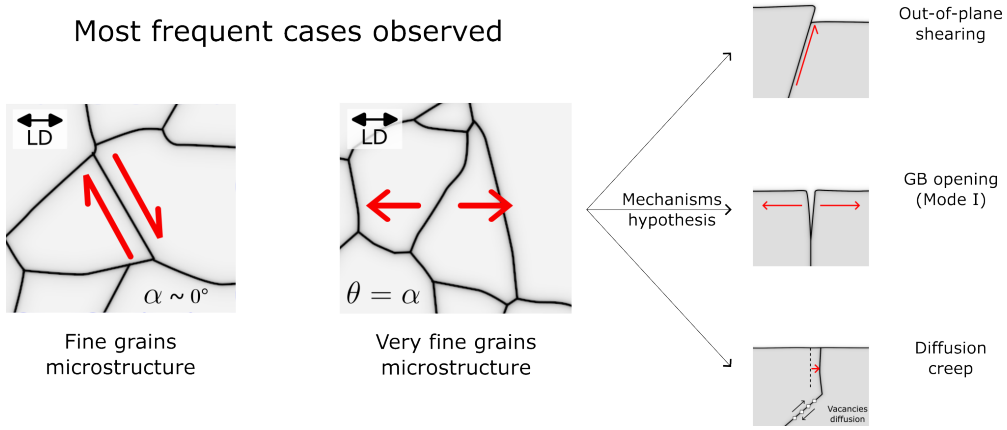

Figure 11: Schematically representation of the most frequent grain boundary sliding cases observed. In-plane shearing was observed in the case of the fine-grains microstructure. In the case of the very fine-grains microstructure, the grain boundary sliding is collinear to the loading direction which could be caused by several mechanisms such as out-of plane shearing, GB opening or diffusion creep.

In the case of the coarse-grain microstructure, the low number of GB sliding events makes it hard to visualize but in the case of the fine-grain microstructure, events are clustered around the low α angles and no event is spotted for α angles over 60 °. This indicates a tendency for shearing, as illustrated on Figure 11. In addition, the color code indicates the out-of-plane nature of the sliding. A cold color indicates a low β angle and a warm color a high β angle. For each of the microstructures, no correlation was found between angle β and α or θ. However, from a general point of view, the very fine-grain plot colors are warmer than the fine-grain ones. This indicates that GB sliding in the very fine-grain microstructure has a strong out-of-plane character, leading to significant grain disorientation. In comparison, the GB sliding happening in the fine-grain microstructure is generally in-plane shearing. In the very fine-grains microstructure, the grain boundary sliding direction was found aligned with the loading direction and out-of plane sliding was observed. This could indicate the occurrence of different mechanisms: (i) Out-of-plane shearing which could be caused by grain rotation; (ii) Mode I GB opening; (iii) Diffusion creep is also plausible looking at the strain rate of the tests. Finally, no correlation was found between the orientation of the GBs, their sliding direction and their sliding amplitude.

3.4. Grain boundary sliding assisted by intragranular slip

Several cases of GB sliding assisted by slip localization in adjacent grains were observed in the HR-DIC results of the coarse- and fine-grain microstructures. In this section, only the coarse- and fine-grain microstructures are studied due to the few slip bands at the interior of grains in the very fine-grain microstructure. Previous HR-DIC measurements on nickel-based superalloys at room temperature [38, 39] evidenced repeatable in-plane strain distribution patterns along the slip bands. The most common distribution is a bell-shaped distribution (Type I). The maximum slip amplitude is nearly at the middle of the slip band, and the extremities show nearly zero slip amplitude. The other type of distribution is logarithmic-like (Type II). The slip amplitude is nearly zero on one end and a plateau at the maximum slip amplitude on the other end. In the present study, very few Type I distribution events were found. The only few Type I events captured are events in the center of grains with low slip amplitude. Once a slip band interacts with a HAGB, the slip amplitude distribution along the slip band is Type II. As the length of the slip bands increases with the slip amplitude, Type II events are the only strain distribution events observed for the most intense slip bands. At room temperature, this strain distribution type was associated with the pile-up mechanism and caused strain concentration in a small volume on the other side of the GB. At 650 °C, numerous behaviors were observed and documented in Figure 12. On the latter, for each mechanism, the following information is plotted: the strain map of the interaction and the direction of the Burgers vector of the incoming slip band; the corresponding EBSD map; and a topography surface plot with EBSD and misorientation data overlaid. Each mechanism presented in this figure was

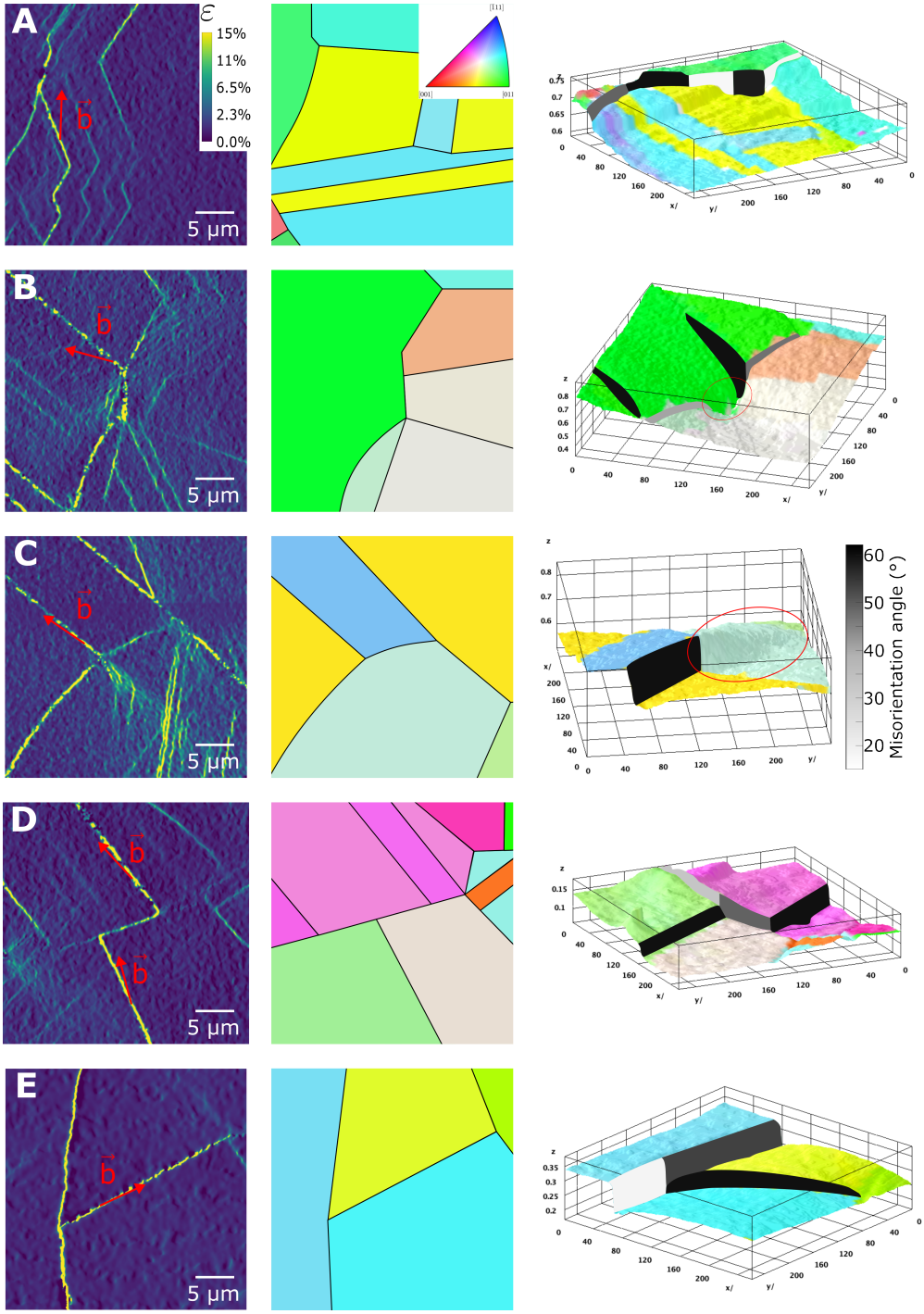

Figure 12: Interaction between slip bands and grain boundaries configurations. For each case, the strain map (left), the corresponding EBSD map (middle), and a 3D plot of the topography of the sample on which the EBSD and the misorientation are overlaid (right) are plotted.

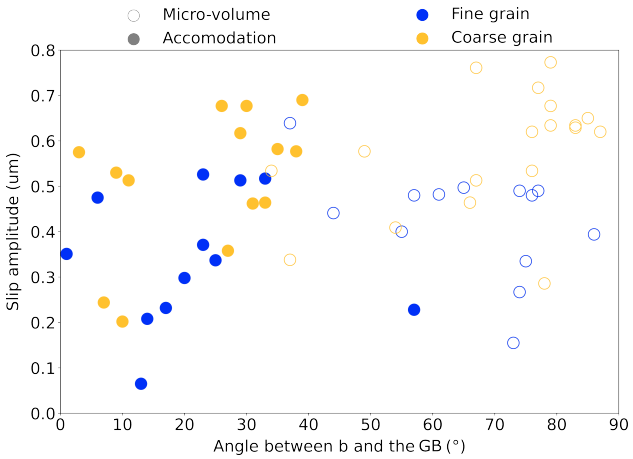

Figure 13: Plot of the slip amplitude of an incoming slip band towards a grain boundary as a function of the angle between the direction of the Burgers vector of the slip band and the trace of the grain boundary plane.

identified for both the fine and coarse grain microstructures. Thus, cases shown are randomly picked from one of the two microstructure results. Two categories can be drawn from these mechanisms:

1. **Grain boundary accommodation**: This category covers cases where no stress concentration is observed on the other side of the GB (A, D, and E from Figure 12). In the A configuration, the incoming slip band induces an additional step in the GB slip amplitude. The slip amplitude distribution is of the Type II kind. As a result, the slip amplitude is maximum at the intersection of the GB and the slip band. The deformation carried by the slip band appears to be transferred to a portion of the GB. In the D configuration, two slip bands are triggered near two well-aligned TBs in neighboring grains. The GB between these slip bands is strained, but the rest of the GB is not. In this case, it appears that the GB acts as a channel, facilitating slip transmission from one grain to the next. Indeed, the two Burgers vectors, as well as the slip planes, are well aligned, which is a favored condition for slip transmission, according to Luster and Morris [40]. They introduced the m' factor defined as follows: $m' = (d_1.d_2)(n_1.n_2)$ where d_1 and d_2 are the Burgers vectors direction of the incoming and outgoing slip system respectively. n_1 and n_2 are the normal to the incoming and outgoing slip planes. A m' factor close to 1 indicates a favored condition for slip transmission. In the D configuration, the m' factor is higher than 0.8. In the E configuration, the incoming slip band has a Type I slip amplitude distribution. The mechanism appears to be morphological rather than slip transfer, unlike the A configuration. There were three such cases observed, one on the fine grain microstructure and two on the coarse grain microstructure. In these cases, sliding amplitude at the GB is much greater than the one of the slip band. The hypothesis that was made here is that the GB sliding is triggered first. The stress/strain state of the boundary allows accommodating the deformation of the slip band. This is in agreement with previous modeling work on FCC materials [41] showing that a high shear stress on GB requires a high shear stress on the slip plane for slip transmission to occur.
2. **Formation of volumes of non-slip localized strain**. This category includes cases where non-slip strain is detected in a small volume near the slip band/GB intersection (B and C in Figure 12). The C configuration was observed at room temperature and generally called micro-volumes in the literature [42]. These were also observed with Type II slip amplitude distribution at room temperature [39]. In the B configuration, the volume is shaped like a sink around a portion of a GB. It has been chosen to classify it in the same category as the micro-volumes because it introduces a non-slip strain localization. In this case, the direction of the slip transmitted to the GB portion is orthogonal to the GB plane. From geometrical assessments, if the GB is vertical and the incoming slip orthogonal to the GB portion, the shear along the GB is complicated. One possibility that remains is the GB opening.

Several parameters influence the occurrence of one configuration or another. Kacher et al. [43] listed a number of parameters that can affect the slip transfer. Among them stands geometric criteria such as the Luster and Morris criterion or the direction of the Burgers vector; crystallographic criterion describing favored slip transfer to slip systems

with the maximum Resolved Shear Stress and Schmid factor; criteria on the GB itself such as its stress state or the GB type and its associated interfacial energy. In the present work carried out at 650 °C, the occurrence of volumes of non-slip localized strain was found to be correlated to the geometric criterion $\vec{b} \wedge \vec{gb}$. It is the angle between the cumulative Burgers vector $\vec{b}$ of the incoming slip band and the trace of the GB, $\vec{gb}$. This correlation is imaged with the plot on Figure 13. In this figure, the cases of interaction between slip bands and GBs found in the coarse- and fine-grain microstructures are exposed. The cases were classified as 'Accommodation' or 'Micro-Volume' following the criteria exposed in the previous section and exposed in Figure 12. Cases of slip transmission assisted by GB sliding (Figure 12.D) have been excluded for the plot of Figure 13. Also, the E cases from Figure 12 were considered as exceptions and were not plotted. In both cases, a high angle between $\vec{b}$ and $\vec{gb}$ results in the formation of a volume of non-slip localized strain at the intersection of the slip band and the GB (B and C cases in Figure 12). At low $\vec{b} \wedge \vec{gb}$ angle, the dominant mechanism is the accommodation of the slip by the GB (A case in Figure 12). The transmission area is located around 40 °. In addition, no dependency to the slip amplitude of the incoming slip band was found.

4. DISCUSSIONS

4.1. Impact of strain localization on tensile properties at 650 °C under protective environment

As foreseen by the Hall-Petch law, the tensile tests performed at 650 °C under vacuum (Figure 3) showed that, in the case of Alloy 718 and in the grain-size range of 12 to 100 μm, the finer the grain size, the greater the yield strength and the more ductile the monotonic tensile behavior. Furthermore, the very fine grain microstructure exhibited a different plastic behavior with a much more pronounced softening after the ultimate tensile strength compared to the fine grain and coarse grain microstructure. This difference in macroscopic tensile behavior can be explained by change in deformation mechanisms, viscous deformation being more pronounced for the very-fine grain microstructure. It was also demonstrated in the present study that the very fine grain microstructure is more prone to grain boundary sliding compared to the two other microstructures. The statistical analysis performed in the present study offers a new approach to explain this monotonic tensile behavior. The strain localization and partitioning were investigated on three microstructures with three different grain sizes to better understand the role of the grain size on the strain localization distribution at the microstructure scale. In addition, special focus has been placed on the interaction of slip bands with grains boundaries. As predicted by atomistic simulations [44], it was found that a fine grain size localizes plasticity at GBs and coarser grain size develops intragranular slip activity.

The statistical analysis of thousands of strain localization events identified and labelled on strain maps reveals that, for finer-grain microstructure, microplasticity is more located at GBs. Indeed, for the three grain sizes studied, in the very fine-grain microstructure, 73 % of the microplasticity is located at GBs versus 42 % and 22 % for the fine- and coarse-grain microstructures, respectively (Figure 7). This is in good agreement with a preliminary study where the role of GB in the deformation process in Alloy 718 has been evidenced at 650 °C for a microstructural state comparable to the fine-grain microstructure [32]. In this temperature range, GBs are known to have a viscous behavior which can accommodate stress [45]. Thus, a greater amount of strain localization at GBs is responsible for a higher amount of strain accommodation at GBs. This could explain why a finer-grain microstructure with more microplasticity at GBs leads to a higher ductility.

To better understand the differences in strain partitioning between the microstructures, the slip events were further investigated. First, the strain partitioning (Figure 7) showed that the strain localization at TBs at 650 °C is not very sensitive to the grain size. Indeed, the coarse- and fine-grain microstructures have the same amount of microplasticity near TBs and the very fine-grain microstructure sightly less (a fifth versus a third for the coarser-grain microstructure). Second, it was found that the coarser the grains, the more slip bands develop at the interior of grains (Figure 7). An argument that could explain the higher strain localization at the interior of grains could be by the Frank-Read sources theory. The energy required to emit a dislocation from a Frank-Read source is inversely proportional to the grain size. A smaller grain size induces a greater curvature to the dislocation emitting from the Frank-Read source. As a result, developing slip bands in the coarse-grain microstructure requires less energy than developing slip bands in the fine-grain microstructure. This lack of intragranular slip could be a reason for a relocation of the strain at GBs in the case of the very fine-grain microstructure. Third, different characteristics of GB sliding were found between the fine- and very fine-grain microstructures (cf. Figure 10). Shearing mode was found in the fine-grain microstructure. In the case of the very fine microstructure, GB sliding occurs preferably along the loading direction, regardless of the

GB orientation towards the loading direction. This observation indicates that mechanisms other than shearing are involved. Possible options are: (i) GB opening (mode I); (ii) creep mechanisms; (iii) combination of both these. Further investigations are required to identify mechanisms occurring. However, regardless of their nature, these mechanisms provide a higher ability of grain boundaries to slide. Indeed, in addition to be aligned along the loading direction, the GB sliding happening in the very fine-grain microstructure is also statistically more out-of-plane. These finding suggest that the GB sliding happening in the very fine-grain microstructure allows a great strain accommodation, which could contribute to the enhancement of the ductility.

As aforementioned, it was found that the GBs sliding has different characteristics in the fine- and very fine-grain microstructures. Unlike the fine-grain microstructure, in the very fine-grain case, the slip direction is preferably along the loading direction (Figure 10). This might be explained by the interaction between GBs and surrounding slip bands, which affects the deformation landscape. Several configurations were found on the fine- and coarse-grain microstructures (Figure 12), and two categories were drawn. The first one is the accommodation of the slip bands by the GBs, and the second one is the formation of a volume of non-slip localized strain within the same grain or in the adjacent grain. The classification of a configuration into one of the two categories was found to be dictated by the angle between the direction of slip and the GB plane (Figure 13). A slip band highly misaligned with the GB plane tends to not be accommodated by the GB, and a volume of non-slip localized strain is formed. On the contrary, a slip band quite aligned with the GB plane is accommodated by the GB. The separation between the two mechanisms is happening at an angle around 40 °. Other interactions mechanisms were spotted, such as slip transmission assisted by GB sliding (Figure 12.D) or slip accommodation by highly strained GBs (Figure 12.E). All these interactions add another component to the GB sliding that can deviate the GBs sliding from the loading direction. According to previous modeling work showing that a higher shear stress on GBs results in less slip transmission [41], it is expected to have more strain accommodation by the GBs with the increasing stress. This might add weight to the previous point made, saying that a finer-grain microstructure with more microplasticity at GBs leads to a higher ductility.

4.2. Role of strain localization on the loss of ductility with air exposure at 650 °C

The influence of the environment on tensile properties was investigated at 650 °C. The specimens subjected to tensile test in an air environment exhibit a great loss in ductility compared to the specimens tested under vacuum. This ductility loss is yet greater for the fine- and very fine-grain microstructures compared to the coarse-grain microstructure (16 % versus 10 %). In addition, the fracture surface analysis indicates that each microstructure exhibits partially intergranular fracture mode. Again, the fine- and very fine-grain microstructures have a greater fraction of intergranular fracture (28 % and 29 % versus 18 %). In the OAIC field, the intergranular fracture has been associated to the loss of ductility [46, 47]. A greater amount of intergranular fracture could thus be responsible for a greater loss of ductility.

The H-DIC results exposed in the previous section showed that a microstructure with fine grains leads to more strain localization at GBs than a microstructure with coarser grains. However, under vacuum, all the microstructure variants show intragranular fracture mode. Some GBs are under intense strain, but the crack does not initiate there nor propagates along them. Thus, this work suggests that the strain state at GBs alone is not responsible for intergranular cracking, but it influences their embrittlement in an oxidative environment due to dynamic mechano-chemical coupling. The mechanisms responsible for this GB embrittlement remains unclear, but the OAIC community seems to agree on a two-range oxygen effect. A review on this subject mentions a short distance effect with the formation of oxides at GBs and a long distance effect caused by the diffusion of oxygen and/or vacancies at GBs that can create embrittling elements [1]. These mechanisms affect conventional GB significantly more than TBs due to difference in crystal symmetry and defects between GBs and TBs [25]. The finer the grain size, the higher the density of GB. Thus, a fine-grain microstructure is statistically more prone to oxygen diffusion and GB embrittlement than a coarse-grain microstructure. This could explain the difference in ductility loss between the coarse-grain microstructure and the fine- and very fine-grain microstructures. In addition, although the crack initiation is intergranular for all the microstructure variants, the propagation is different. According to the tensile curves (Figure 3), the fracture surfaces of the fine- and very fine-grain microstructures appear more brittle than the one of the coarse-grain microstructure. Again, according to a previous work on steel [48], this is due to the grain size. A finer grain size reduces the ductile-brittle transition.

However, the fine and very fine-grain microstructures have different strain partitioning but similar ductility loss. If the ductility loss were to depend only on the grain size, the ductility loss of the very fine-grain microstructure should be

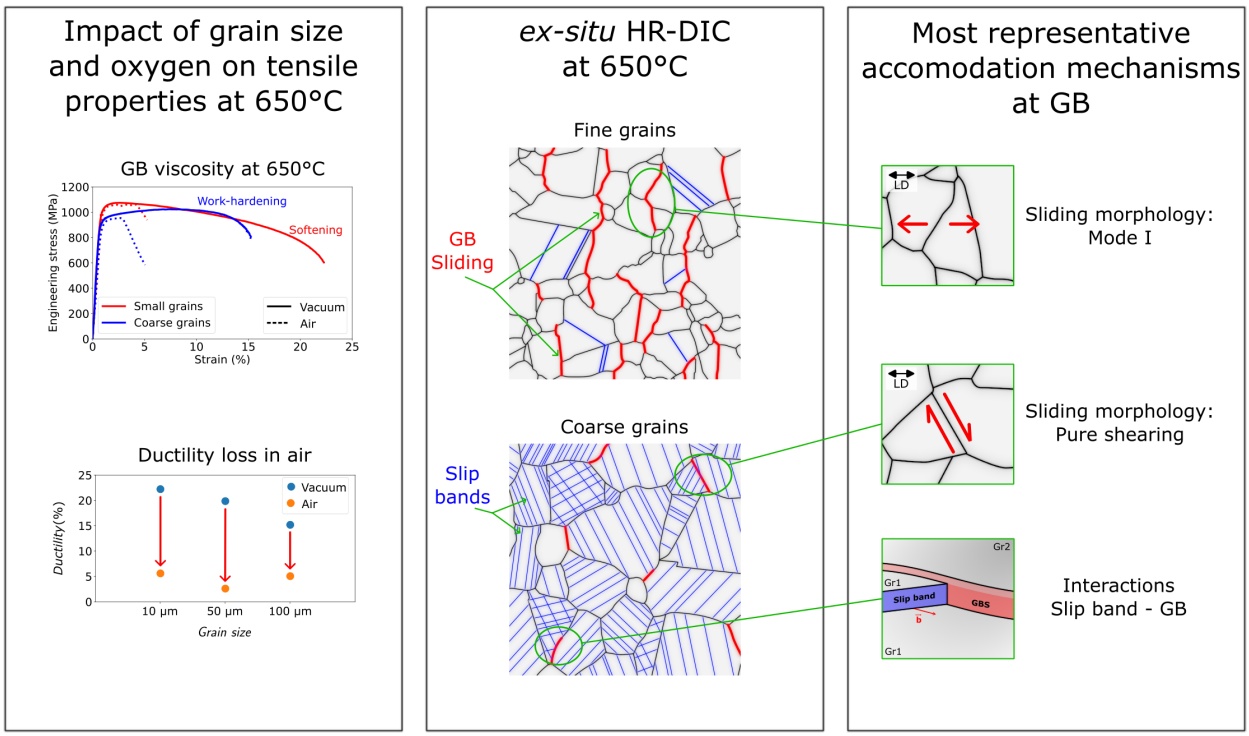

Figure 14: Multi-scale representation of the impact of strain localization on tensile properties.

higher than the fine one. Indeed, the very fine-grain microstructure as 1.68 times more GBs than the fine-grain microstructure. Depending on the referential, the strain partitioning and GB sliding mechanisms either limit the ductility loss of the very fine-grain microstructure or enhance the one of the fine-grain microstructure. On one hand, it seems less likely that the GB sliding happening in the very fine-grain microstructure limits the ductility loss. GB opening inherent to creep mechanisms both tend to increase the diffusion rate of the oxygen in the microstructure. The first due to oxide cracking at the oxide tip and/or gas transportation/surface diffusion, and the second due to vacancies transportation. On the other hand, the ductility loss of the fine and coarse-grain microstructures could be enhanced by the interactions between slip bands and GBs. In the case where the GB accommodates the slip band (Figure 12.A), the cumulated Burgers vector of the dislocations carried by the slip band is not exactly aligned with the GB plane. Thus, these dislocations will interact with the GB, and interactions at the dislocation level will depend on the intrinsic properties of the GB. One of the possibilities is the creation of defects such as vacancies in the GB, which can facilitate the diffusion of oxygen. In the case where the GB does not accommodate the strain carried by the slip band, one of the outcomes is the GB opening (Figure 12.B). This case was directly observed on the fracture surface of the fine-grain microstructure (cf. Figure 6.F). Some of these slip band/grain boundary accommodation mechanisms are reported in the literrature review based on in-situ TEM nanomechanical testing [49]. Even if hypotheses are drawn, the link between early strain localization and fracture under air remains unclear. Further research is needed to fill the gap between early strain localization and fracture behavior.

5. CONCLUSIONS

HR-DIC measurements were performed on interrupted tensile tests at 650 °C on three microstructures with different grain sizes. Statistical analyses of thousands of plastic events each showed significant differences in strain localization depending on the grain size. At 650 °C, a finer-grain microstructure leads to a higher strain localization at grain boundaries (GBs) when the strain on the coarse grain microstructure is mostly localized in the form of

intragranular slip bands and slip near Σ3 twin boundaries. The higher ductility of the fine-grain microstructure was associated with the ability of the GBs to accommodate the strain and the lower intensity of intragranular slip due to constraint lengths. The study of specific cases of interactions of slip bands with GBs revealed that GBs accommodate slip bands when the cumulated Burgers vector of the incoming slip band and the GB have a misalignment lower than 40 °. In addition, tensile tests up to fracture were performed in air, and fracture surfaces were analyzed. It was found that a smaller grain size leads to a higher fraction of intergranular cracking and a greater reduction in ductility. A schematic illustration of the interplay role of strain localization at the microstructure scale, grain size, tensile behavior and ductility, summarizing the main findings of the present work, is shown in Fig. 14. The hypothesis of oxidation assisted intergranular cracking (OAIC) drawn from these results is that in air and at 650 °C the damaging process is driven by mechano-chemical coupling. It is highly sensitive to the fraction of GBs due to intense strain localization and their ability to act as a preferential diffusion path. This sensitivity to intergranular cracking is expected to be strain-rate dependent and would be of great interest for further investigations.

6. ACKNOWLEDGEMENTS

This work was supported by the European Research Council [project HT-S_4DefOx - Grant number 948007]. The authors are grateful to the *Centre National de la Recherche Scientifique (CNRS)* for the mobility grant with the International Research Project denoted "CIN&MAT". RLB and JCS acknowledge the NSF (award #2338346) for financial support. This work was carried out in part in the Materials Research Laboratory Central Research Facilities at the University of Illinois Urbana-Champaign. The authors particularly acknowledge the Raimond Castaing Microanalysis Centre (UAR 3623) for scanning electron microscopy access.

7. License

8. Data Availability

The raw/processed data required to reproduce these findings cannot be shared at this time, as the data also forms part of an ongoing study.

9. Declaration of competing interests

The authors declare that they have no known competing financial interests or personal relationships that could have appeared to influence the work reported in this paper.

References

[1] A. Pineau and S. Antolovich. Fatigue intergranulaire. *Joints de grains et plasticité cristalline. dir. L. Priester*, pages 225–288, 2011.

[2] T. Sanviemvongsak, D. Monceau, C. Desgranges, and B. Macquaire. Intergranular oxidation of Ni-base alloy 718 with a focus on additive manufacturing. *Corrosion Science*, 170, 2020.

[3] R. H. Bricknell and D. A. Woodford. Embrittlement of Nickel Following High Temperature Air Exposure. *Metallurgical transactions. A, Physical metallurgy and materials science*, 12 A(3):425–433, 1981.

[4] H. H. Smith and D. J. Michel. Effect of Environment on Fatigue Crack Propagation Behavior of Alloy 718 At Elevated Temperatures. *Metallurgical transactions. A, Physical metallurgy and materials science*, 17 A(2):370–374, 1986.

[5] V. Garat, J. Deleume, J-M. Cloué, and E. Andrieu. High temperature intergranular oxidation of alloy 718. *Superalloys 718, 625, 706 and Derivatives*, pages 559–569, 2005.

[6] R. Molins, G. Hochstetter, J.C. Chassaigne, and E. Andrieu. Oxidation effects on the fatigue crack growth behaviour of alloy 718 at high temperature. *Acta Materialia*, 45:663–674, 1997.

[7] H. Ghonem, T. Nicholas, and A. Pineau. Elevated temperature fatigue crack growth in Alloy 718 - Part I: Effects of mechanical varaibles. *Fatigue and Fracture of Engineering Materials and Structures*, 16:565–576, 1993.

[8] E.O. Hall. The Deformation and Ageing of Mild Steel: III Discussion of Results. *Proceeding of the Physical Society. Section B*, 64:747–753, 1951.
[9] N.J. Petch. The Cleavage Strength of Polycrystals. *Journal of the Iron and Steel Institute*, 174:25–28, 1953.
[10] Roberto B. Figueiredo, Megumi Kawasaki, and Terence G. Langdon. Seventy years of hall-petch, ninety years of superplasticity and a generalized approach to the effect of grain size on flow stress. *Progress in Materials Science*, 137:101131, 2023.
[11] J.F. Nye. Some geometrical relations in dislocated solids. *Acta Metallurgica*, 1:153–162, 1953.
[12] S. Birosca, G. Liu, R. Ding, J. Jiang, T. Simm, C. Deen, and M. Whittaker. The dislocation behaviour and gnd development in a nickel based superalloy during creep. *International Journal of Plasticity*, 118:252–268, 2019.
[13] Y. Guo, T.B. Britton, and A.J. Wilkinson. Slip band–grain boundary interactions in commercial-purity titanium. *Acta Materialia*, 76:1–12, 2014.
[14] Marissa A. Linne, Thomas R. Bieler, and Samantha Daly. The effect of microstructure on the relationship between grain boundary sliding and slip transmission in high purity aluminum. *International Journal of Plasticity*, 135:102818, 2020.
[15] Wujun Yin, Fabien Briffod, Haoyu Hu, Takayuki Shiraiwa, and Manabu Enoki. Three-dimensional configuration of crystal plasticity in stainless steel assessed by high resolution digital image correlation and confocal microscopy. *International Journal of Plasticity*, 170:103762, 2023.
[16] Jutian Chen, Junxia Lu, Wang Cai, Yuefei Zhang, Yongfeng Wang, Wenxiang Jiang, Muhammad Rizwan, and Ze Zhang. In-situ study of adjacent grains slip transfer of Inconel 718 during tensile process at high temperature. *International Journal of Plasticity*, 163:103554, 2023.
[17] R.L. Black, D. Anjaria, J. Genée, V. Valle, and J.C. Stinville. Micro-strain and cyclic slip accumulation in a polycrystalline nickel-based superalloy. *Acta Materialia*, 2024.
[18] C. C. Tasan, J. P.M. Hoefnagels, M. Diehl, D. Yan, F. Roters, and D. Raabe. Strain localization and damage in dual phase steels investigated by coupled in-situ deformation experiments and crystal plasticity simulations. *International Journal of Plasticity*, 63:198–210, 2014.
[19] Adrien Guery, François Hild, Félix Latourte, and Stéphane Roux. Slip activities in polycrystals determined by coupling DIC measurements with crystal plasticity calculations. *International Journal of Plasticity*, 81:249–266, 2016.
[20] Yongjun Guan, Bo Chen, Jinwen Zou, T. Ben Britton, Jun Jiang, and Fionn P.E. Dunne. Crystal plasticity modelling and HR-DIC measurement of slip activation and strain localization in single and oligo-crystal Ni alloys under fatigue. *International Journal of Plasticity*, 88:70–88, 2017.
[21] Haoyu Hu, Fabien Briffod, Takayuki Shiraiwa, and Manabu Enoki. Automated slip system identification and strain analysis framework using high-resolution digital image correlation data: Application to a bimodal Ti-6Al-4V alloy. *International Journal of Plasticity*, 166:103618, 2023.
[22] F. Bourdin, J.C. Stinville, M.P. Echlin, P.G. Callahan, W.C. Lenthe, C.J. Torbet, D. Texier, F. Bridier, J. Cormier, P. Villechaise, T.M. Pollock, and V. Valle. Measurements of plastic localization by heaviside-digital image correlation. *Acta Materialia*, 157:307–325, 2018.
[23] J.H. Liu, N. Vanderesse, J.-C. Stinville, T.M. Pollock, P. Bocher, and al. IN-PLANE and out-of-plane deformation at the SUB-GRAIN scale in polycrystalline materials assessed by confocal microscopy. *Acta Materialia*, 169:260–274, 2019.
[24] Y. Jin, M. Bernacki, A. Agnoli, B. Lin, GS. Rohrer, AD. Rollett, and N. Bozzolo. Evolution of the annealing twin density during δ-supersolvus grain growth in the nickel-based superalloy inconel™ 718. *Metals*, 6:1–5, 2016.
[25] Ph. E.-G. Wagenhuber, V. B. Trindade, and U. Krupp. The Role of Oxygen-Grain-Boundary Diffusion During Intercrystalline Oxidation and Intergranular Fatigue Crack Propagation in Alloy 718. *Superalloys 718, 625, 706 and Derivatives*, pages 591–600, 2005.
[26] R. Jiang, F. Pierron, S. Octaviani, and P.A.S. Reed. Characterisation of strain localisation processes during fatigue crack initiation and early crack propagation by SEM-DIC in an advanced disc alloy. *Materials Science and Engineering: A*, 699, 2017.
[27] J.C. Stinville, W.C. Lenthe, M.P. Echlin, P.G. Callahan, D. Texier, and T.M. Pollock. Microstructural statistics for fatigue crack initiation in polycrystalline nickel- base superalloys. *International Journal of Fracture*, 208:221–240, 2017.
[28] D. Texier, J. Cormier, P. Villechaise, and al. Crack initiation sensitivity of wrought direct aged alloy 718 in the very high cycle fatigue regime: the role of non-metallic inclusions. *Mater Sci Eng A*, 678:122–136, 2016.
[29] M.A. Charpagne, J. Hestroffer, A.T. Polonsky, M.P. Echlin, Damien Texier, and al. Slip localization in Inconel 718: a three-dimensional and statistical perspective. *Acta Materialia*, 215, 2021.
[30] JC Stinville, N Vanderesse, F Bridier, P Bocher, and TM Pollock. High resolution mapping of strain localization near twin boundaries in a nickel-based superalloy. *Acta Materialia*, 98:29–42, 2015.
[31] Dylan Agius, Anna Kareer, Abdullah Al Mamun, Christopher Truman, David M. Collins, Mahmoud Mostafavi, and David Knowles. A crystal plasticity model that accounts for grain size effects and slip system interactions on the deformation of austenitic stainless steels. *International Journal of Plasticity*, 152:103249, 2022.
[32] Damien Texier, Julien Milanese, Malo Jullien, Julien Genée, Jean-Charles Passieux, Didier Bardel, Eric Andrieu, Marc Legros, and Jean-Charles Stinville. Strain localization in the alloy 718 ni-based superalloy: From room temperature to 650 °c. *Acta Materialia*, 268:119759, 2024.
[33] Kai Shang Li, Run Zi Wang, Xian Cheng Zhang, and Shan Tung Tu. Creep-fatigue damage mechanisms and life prediction based on crystal plasticity combined with grain boundary cavity model in a nickel-based superalloy at 650°C. *International Journal of Plasticity*, 165:103601, 2023.
[34] Li Jianwei, Ding Chaogang, Chen Wanji, Shan Debin, Guo Bin, and Xu Jie. Strain localization and ductile fracture mechanism of micro/mesoscale deformation in ultrafine-grained pure copper. *Materials Design*, 229, 2023.
[35] K. Cave, D. Texier, E. Fessler, D. Monceau, and D. Poquillon. Size effect on the tensile mechanical behavior of thin Ti6242S specimens at 723 K and 823 K. *Metallurgical and Materials Transactions A: Physical Metallurgy and Materials Science*, 54(2):549–561, 2023.
[36] Marie-Agathe Charpagne, Jean-Charles Stinville, Andrew Polonsky, M. Echlin, and T. Pollock. A Multi-modal Data Merging Framework for Correlative Investigation of Strain Localization in Three Dimensions. *JOM*, 2021.
[37] J. Schindelin, I. Arganda-Carreras, E. Frise, V. Kaynig, M. Longair, T. Pietzsch, S Preibisch, C. Rueden, S Saalfeld, B. Schmid, J.-Y. Tinevez, D. James White, V. Hartenstein, K. Eliceiri, P. Tomancak, and A. Cardona. Fiji: an open-source platform for biological-image analysis. *Nature Methods*, 9(7):676–682, 2012.

[38] R. Sperry, A. Harte, J. Quinta da Fonseca, E. R Homer, R. H Wagonerand, and D. T Fullwood. Slip band characteristics in the presence of grain boundaries in nickel-based superalloy. *Acta Materialia*, pages 229–238, 2020.
[39] R.L. Black, T. Garbowski, C. Bean, and et al. High-Throughput High-Resolution Digital Image Correlation Measurements by Multi-Beam SEM Imaging. *Exp Mech*, page 939–953, 2023.
[40] J. Luster and M.A. Morris. Compatibility of deformation in two-phase Ti-Al alloys: Dependence on microstructure and orientation relationships. *Metall Mater Trans A*, 26:1745–1756, 1995.
[41] M. P. Dewald and W. A. Curtin. Multiscale modelling of dislocation/grain boundary interactions. II. Screw dislocations impinging on tilt boundaries in Al. *Philosophical Magazine*, 87:4615–4641, 2007.
[42] P. Villechaise, J. Cormier, T. Billot, and J. Mendez. Mechanical behaviour and damage processes of UDIMET 720Li: Influence of localized plasticity at grain boundaries. *Superalloys 2012*, pages 15–24, 2012.
[43] Josh Kacher, B.P. Eftink, B. Cui, and I.M. Robertsons. Dislocation interactions with grain boundaries. *Current Opinion in Solid State and Materials Science*, 18:227–243, 2014.
[44] S.S. Rajaram, A. Gupta, and G.B. et al. Thompson. Grain-Size-Dependent Grain Boundary Deformation during Yielding in Nanocrystalline Materials Using Atomistic Simulations. *JOM*, 72:1745–1754, 2020.
[45] A.P. Sutton and R.W. Balluffi. *Interfaces in Crystalline Materials*. Oxford, 1995.
[46] Eric Andrieu, Bertrand Max, and Bernard Viguier. Oxidation Assisted Intergranular Cracking in Alloy 718: Effects of Strain Rate and Temperature. *AerospaceLab-journal*, 9(August):1–7, 2015.
[47] M.C. Rezende, L.S. Araújo, S.B. Gabriel, J. Dille, and L.H. de Almeida. Oxidation assisted intergranular cracking under loading at dynamic strain aging temperatures in Inconel 718 superalloy. *Journal of Alloys and Compounds*, 643:256–259, 2015.
[48] J.W. Morris. The influence of grain size on the mechanical properties of steel. *Lawrence Berkeley National Laboratory*, 2001.
[49] Q. Yu, M. Legros, and A. M. Minor. In situ TEM nanomechanics. *MRS Bulletin*, 40(1):62–70, 2015.